RSC Advances

ROYAL SOCIETY OF CHEMISTRY

PAPER

View Article Online
View Journal | View Issue

Check for updates

Cite this: *RSC Adv.*, 2024, **14**, 7221

Efficient photoactivated hydrogen evolution promoted by Cu_xO–gCN–TiO_2–Au (x = 1,2) nanoarchitectures†

Mattia Benedet,[ab] Gian Andrea Rizzi,[ab] Alberto Gasparotto,[ab] Lunjie Zeng,[c] Gioele Pagot,[d] Eva Olsson,[c] Vito Di Noto,[d] Chiara Maccato[*ab] and Davide Barreca[b]

Received 30th January 2024
Accepted 23rd February 2024

DOI: 10.1039/d4ra00773e

rsc.li/rsc-advances

In this work, we propose an original and potentially scalable synthetic route for the fabrication of Cu_xO–gCN–TiO_2–Au (x = 1,2) nanoarchitectures, based on Cu foam anodization, graphitic carbon nitride liquid-phase deposition, and TiO_2/Au sputtering. A thorough chemico-physical characterization by complementary analytical tools revealed the formation of nanoarchitectures featuring an intimate contact between the system components and a high dispersion of gold nanoparticles. Modulation of single component interplay yielded excellent functional performances in photoactivated hydrogen evolution, corresponding to a photocurrent of ≈ -5.7 mA cm^{-2} at 0.0 V *vs.* the reversible hydrogen electrode (RHE). These features, along with the very good service life, represent a cornerstone for the conversion of natural resources, as water and largely available sunlight, into added-value solar fuels.

1 Introduction

The progressively higher global demand of energy, whose supply is still predominantly dependent on fossil fuels, and the resulting climate changes aggravation are the motivating forces for numerous efforts aimed at achieving alternative and sustainable solutions.[1–7] In this regard, sunlight-driven water splitting to yield molecular hydrogen (H_2), a zero-emission and renewable energy vector, stands as a strategic choice for the conversion of an inexhaustible natural resource into chemical energy,[8–17] provided that a careful selection and engineering of active semiconductor photoelectrocatalysts is performed.[7,10,12,18,19] Among the possible candidates for the hydrogen evolution reaction (HER), an effective and spotless process to deliver hydrogen,[5] p-type copper oxides (Cu_xO, x = 1,2; $E_g \approx 2.1$ and ≈ 1.5 eV for x = 1 and 2, respectively) are inexpensive, non-toxic and naturally abundant semiconductors featuring efficient sunlight harvesting.[1,10,12,20–23] In particular, CuO has also been proposed as a Cu_2O overlayer to achieve an improved charge carrier transport towards the electrolyte, suppressing the detrimental recombination of photogenerated electrons and holes. In addition, CuO/Cu_2O systems feature an extended spectral absorption compared to Cu_2O,[2,13,14] allowing thus an enhanced harvesting of the incoming electromagnetic radiation.

To further improve charge transfer kinetics and overcome instability problems due to photocorrosion,[1,14,16,17,23] different literature works have so far been focused on the *ad hoc* modification of Cu_xO surface with adequate partners, to yield nanoheterojunctions providing supplementary benefits.[1,13,20] To this aim, graphitic carbon nitride (gCN), a burgeoning n-type semiconductor possessing a two-dimensional structure ($E_g \approx 2.7$ eV), presents several concurrent advantages, including cost effectiveness, eco-friendly character, stability, tuneable electronic structure, and attractive photoactivity.[4,11,19,24–27] The system performances can be further improved by the additional introduction of oxide semiconductors and/or metals, obtaining multi-component functional nanoarchitectures.[9,12] In particular, TiO_2 can exert a protective action against Cu_xO photocorrosion, limit the undesired recombination of photocarriers affecting gCN, and boost charge mobility at the photoelectrocatalyst–electrolyte interface.[3,8,15,17,18,21,28,29] The latter advantage can be favourably amplified by functionalizing the target systems with low amounts of optimally dispersed Au nanoparticles (NPs), acting as electric/catalytic/optical mediators for the achievement of efficient H_2 generation.[9,15,23,25,26]

In the present study, we propose for the first time the fabrication of Cu_xO–gCN–TiO_2–Au (x = 1,2) nanoarchitectures through an original multi-step synthetic strategy (Fig. 1a; see

---

[a] *Department of Chemical Sciences, Padova University and INSTM, 35131 Padova, Italy. E-mail: chiara.maccato@unipd.it*

[b] *CNR-ICMATE and INSTM, Department of Chemical Sciences, Padova University, 35131 Padova, Italy*

[c] *Department of Physics, Chalmers University of Technology, 41296 Gothenburg, Sweden*

[d] *Section of Chemistry for the Technology (ChemTech), Department of Industrial Engineering, Padova University and INSTM, 35131 Padova, Italy*

† Electronic supplementary information (ESI) available. See DOI: https://doi.org/10.1039/d4ra00773e

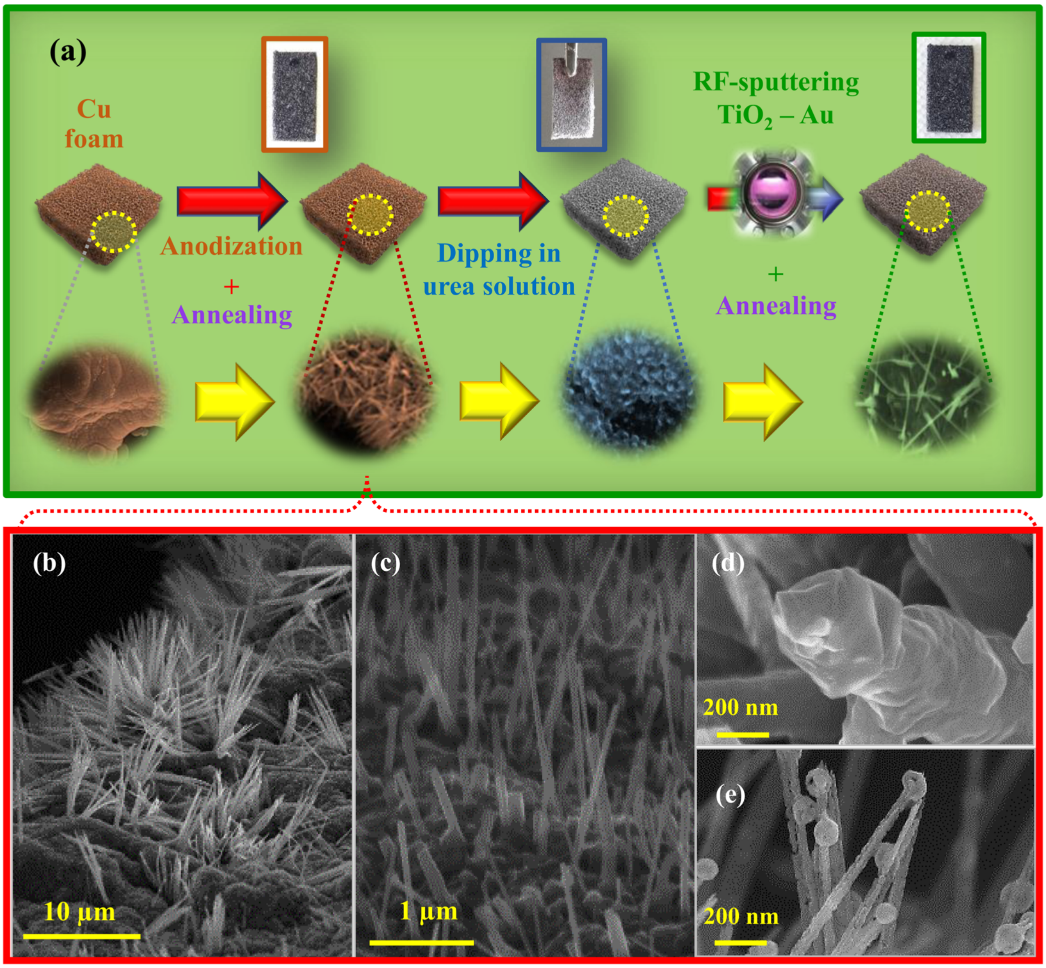

Fig. 1 (a) Sketch of the preparation route to Cu_xO–gCN–TiO_2–Au ($x = 1,2$) photoelectrocatalysts used in the present work. (b–e) Representative field emission-scanning electron microscopy (FE-SEM) micrographs for Cu_xO systems.

also the ESI†). Metallic Cu foams, offering high porosity and electrical conductivity, as well as electrolyte accessibility and efficient release of gaseous products,[6,30] are initially subjected to anodization and subsequent thermal treatment in air for the *in situ* growth of Cu_xO.[22,31] The proposed route affords quasi-1D nanostructures with a high active area, promoting, in turn, a homogeneous distribution of gCN, whose deposition was carried out by dipping in urea-containing solutions, followed by annealing.[10] The eventual introduction of TiO_2 and Au NPs was performed by sequential radio frequency (RF)-sputtering, carried out under mild conditions to avoid alterations of the underlying system nano-organization. The target specimens are characterized by an enhanced mechanical stability in comparison to electrocatalysts obtained by immobilization of inks/pastes with additives/binders on various substrates.[4,5,7,11,19,28] In addition, the synergy between the RF-sputtering infiltration power and the high area morphology[30,32] of the pristine Cu_xO–gCN enabled an intimate contact between the single components, and an efficient dispersion of Au NPs. Altogether, these features yielded, for Cu_xO–gCN–TiO_2–Au photoelectrocatalysts, a photocurrent density of ≈ -5.7 mA cm^{-2} at 0.0 V *vs.* RHE and a Tafel slope of ≈ -160 mV dec^{-1}, among the best ever reported in the literature up to date for homologous Cu_xO- and/or gCN-containing systems in such applications.

2 Experimental

2.1 Material preparation

2.1.1 Cu foams anodization. The growth of Cu_xO on copper foam substrates (Cu-4753, RECEMAT BV; lateral size = 1 cm × 2 cm) was carried out basing on a previously reported electrochemical anodization route.[33] After an initial treatment in 1.5 M HCl for 5 min and rinsing in deionized water, Cu foams were anodized by immersion in a 1.0 M KOH solution for 20 min at 10 mA. Subsequently, each sample was washed twice with deionized water and finally dried at room temperature. For the preparation of bare Cu_xO specimens, the anodized Cu foam was subjected to a two-step thermal treatment in air (300 °C for 1 h, and 450 °C for 2 h), finally yielding a dark grey material.

2.1.2 Functionalization with gCN. 4.0 g of urea (Thermo-Fisher, 98+%) were dispersed in a 20 mL solution of acetonitrile/water 80/20 (% v/v). The above specimens were then dipped for 15 min in the obtained solution, maintained under constant stirring at room temperature, and subsequently dried in air for 30 min. The procedure was repeated three times. Preparation of Cu_xO–gCN specimens involved a final two-step annealing procedure composed of a treatment in air at 300 °C for 1 h, and another one in air at 450 °C for 2 h, in order to promote urea thermal condensation to gCN.[10]

2.1.3 Functionalization with TiO_2 and Au nanoparticles. The introduction of TiO_2 and Au in Cu_xO–gCN specimens was performed by RF-sputtering from electronic grade Ar plasmas, using a custom-built two-electrode RF plasmochemical reactor ($\nu = 13.56$ MHz). Titanium (Alfa Aesar®; thickness = 0.3 mm; purity = 99.95%) or gold (BALTEC AG; thickness = 0.1 mm; purity = 99.99%) targets were mounted on the RF electrode, whereas Cu foam-supported Cu_xO–gCN were fixed on the grounded one. Basing on previously obtained results,[32] depositions were carried out using the following settings for TiO_2 (Au) sputtering: Ar flow rate = 10 standard cubic centimeters per minute (sccm); total pressure = 0.30 (0.38) mbar; growth temperature = 60 °C; RF-power = 20 (5) W; overall duration = 150 (20) min. Specimens containing TiO_2 and Au were obtained by sequential deposition of titanium and gold under the indicated conditions. Prior to chemico-physical characterization, materials were annealed in air under the same operating conditions reported above for Cu_xO–gCN. Repeated experiments allowed to ascertain the reproducibility of the adopted synthetic procedure, evidencing that the morphology and size distribution of the different electrocatalyst components were maintained during the implementation of the various preparative steps.

2.2 Characterization

FE-SEM images were collected with a Zeiss Supra 40 VP instrument equipped with an INCA x-act PentaFET Precision spectrometer for energy-dispersive X-ray spectroscopy (EDXS), using primary beam voltages between 10 and 20 kV. X-ray photoelectron spectroscopy (XPS) analyses were carried out with a Specs EnviroESCA apparatus equipped with an AlKα X-ray source ($h\nu = 1486.6$ eV). Binding energy (BE) values (uncertainty = ±0.1 eV) were corrected for charging phenomena by assigning a position of 284.8 eV to the C 1s signal arising from adventitious contamination.[34] Peak fitting was performed using the Keystone software (Specs) and applying a Shirley-type background subtraction.

A JEOL monochromated ARM200F instrument, operated at 200 kV, was used for scanning transmission electron microscopy (STEM) imaging, STEM-EDXS and STEM-electron energy loss spectroscopy (EELS) analyses. The apparatus was equipped with a double-Wien type monochromator, CEOS probe and image C_s correctors, a double silicon drift detector (SDD) for EDXS, and a Gatan image filter (GIF) Continuum for EELS. STEM annular dark field (ADF) images were recorded with beam convergence and inner collection half-angles of ≈27 mrad and ≈50 mrad, respectively.

The system photoelectrocatalytic activity was tested in 0.5 M $KHCO_3$ aqueous solution (Carlo Erba, pH = 8.5), using an Autolab PGSTAT204 potentiostat/galvanostat. The fabricated materials were used as working electrodes, whereas a standard Hg/HgO (MMO) electrode and a Pt wire were used as reference and counter-electrodes, respectively. During each test, the sample was illuminated from the front side (electrode–electrolyte interface) using a white light LED source (intensity ≈ 100 mW cm^{-2}).

Additional details on material preparation and characterization are available in the ESI.†

3 Results and discussion

The system morphology and its interplay with the processing conditions were initially investigated by FE-SEM. As revealed by Fig. 1b–e, the Cu foam anodization and subsequent annealing yielded high area arrays of copper oxide nanowires (average aspect ratio ≈5000 nm/150 nm = 33), some of which featured the presence of spheres (diameter ≈ 100 nm) on their tips. The obtainment of such structures is not controlled by vapor–solid or vapor–liquid–solid mechanisms,[35] but depends on Cu oxidation at the electrode/electrolyte interface during the anodization step, and subsequent Cu_xO nanowires formation upon annealing, as reported by previous investigators.[36–39] FE-SEM images and EDXS results for composite systems, along with pertaining observations, are reported in the ESI (see Fig. S2, S3 and Page S6).†

X-ray diffraction (XRD) measurements for all the target specimens revealed the co-presence of Cu_2O and CuO, along with reflections of metallic copper arising from the Cu foam substrate (Fig. S4†). No appreciable signals originating from gCN, TiO_2, or Au could ever be detected. The lack of diffraction peaks attributable to graphitic carbon nitride was due to its amorphous character (see also below), whereas the absence of titanium dioxide and gold reflections could be traced back to their low amount and high dispersion. On the other hand, gCN, Au and TiO_2 presence was demonstrated by XPS, TEM and related outcomes (see below).

Additional key information on the system chemical composition and elemental oxidation states was provided by XPS analyses (see also Fig. S5†). As a matter of fact, titanium and gold photopeaks were undetectable (see Fig. S6a and b†), indicating thus that TiO_2 and Au were not present in the outermost material regions (compare TEM data and pertaining observations). Irrespective of the analyzed sample, the Cu 2p peak shape and position [Fig. 2a; BE (Cu $2p_{3/2}$) ≈933.8 eV], along with the presence of shake-up satellites, agreed with CuO presence.[1,6,8,10,21,23] Evaluation of copper Auger parameters (see also the ESI and Fig. S6c†) yielded $\alpha = 1851.4$ eV, in agreement with the surface presence of CuO.[34,40–43] The O/Cu atomic percentage (at%) ratio values (1.5–1.6) were higher than the stoichiometric one (1.0) expected for CuO, suggesting the presence of chemisorbed –OH groups and adsorbed H_2O on the system surface. Accordingly, O 1s signals (Fig. 2b) resulted from the concurrence of CuO lattice oxygen (I, BE = 529.9 eV),[21,23] surface chemisorbed –OH groups (II, BE = 531.5 eV),[3,25] and adsorbed water/C–O bonds between gCN and CuO (both contributing to band III, located at BE = 533.0 eV).[10,24] Indeed, –OH presence is beneficial for the target end-use,[1,21] and gCN–CuO bonding is favourable to obtain an improved electron–hole

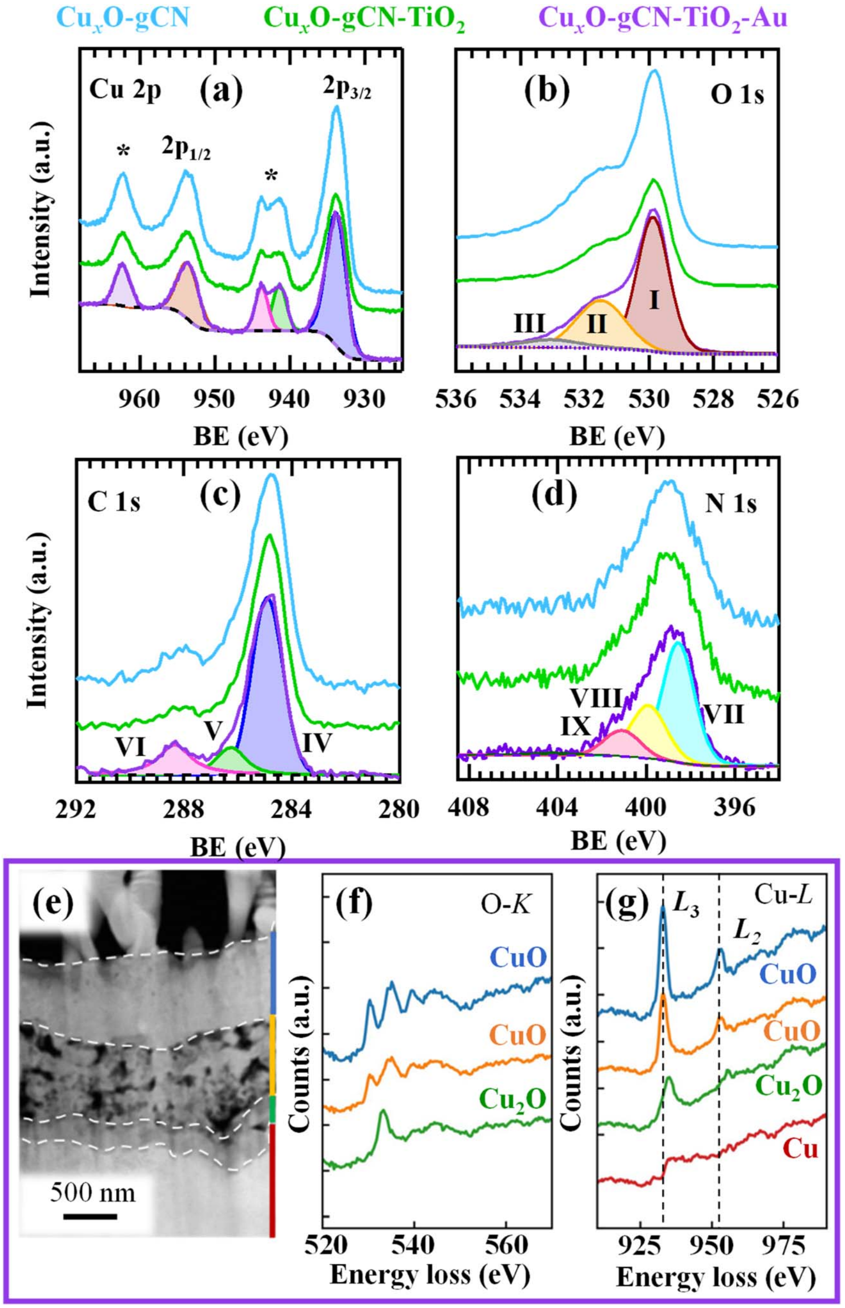

Fig. 2 Cu 2p (a), O 1s (b), C 1s (c), and N 1s (d) photoelectron peaks for Cu_xO–gCN, Cu_xO–gCN–TiO_2, and Cu_xO–gCN–TiO_2–Au. For the latter sample, fit components are displayed along with raw spectra as a representative case. In (a), shake-up satellites are denoted by *. (e) Representative cross-sectional STEM-ADF image for Cu_xO–gCN–TiO_2–Au. Dashed lines mark interfaces between adjacent layers; the middle one is porous, while the others are continuous. The average thickness is ≈1 μm, 1.5 μm, and 200 nm for the top (blue), middle (orange) and bottom (green) layers, respectively. (f and g) Corresponding electron energy loss spectroscopy (EELS) spectra of O-K and Cu-L edges. The positions of Cu $L_{3,2}$ white-lines are marked by dashed lines.

separation,[24] resulting thus in higher functional performances. The C 1s signal (Fig. 2c), beside the adventitious carbon band (IV, BE = 284.8 eV),[3,9,16,25,28] presented a component at ≈286.1 eV (V) due to both C–O bonds and $-C-NH_x$ moieties (x = 1,2) on gCN heptazine ring edges.[3,4,17,24,44] Finally, signal VI at BE ≈ 288.1 eV was attributed to N–C═N carbon atoms in gCN.[1,8,16,18,28] In line with these results, N 1s components (Fig. 2d) were related to bi-coordinated nitrogen (C═N–C; VII, BE = 398.7 eV),[4,8,24,28] tertiary $N-(C)_3$ atoms (VIII, BE = 399.9 eV),[1,8,24,26,28] and $-NH_x$ groups (IX, BE = 401.1 eV).[3,16,28,45]

An important insight into the system nano-organization was gained by TEM and related analyses. Preliminary STEM imaging on Cu_xO–gCN–TiO_2–Au (Fig. 2e) revealed the presence of a stacked structure over the Cu foam, mainly composed of Cu and O, and characterized by diverse layers showing different Cu–O bonding features, as demonstrated by EELS results. In fact, the energy loss near edge structure (ELNES) in EELS is sensitive to variations in local chemical bonding,[46] *i.e.* in copper valence and coordination.[44] In the top two layers (marked in blue and orange in Fig. 2e), the features of O-K and Cu-L ELNES signals supported the presence of CuO,[44] whereas the O-K ELNES of the layer next to Cu substrate (marked in green in Fig. 2e) indicates the occurrence of Cu_2O. The O-K top layer spectrum presented four signals located between ≈530 and 550 eV (Fig. 2f), whereas only an intense peak (530–540 eV) and a broad one (540–550 eV) could be observed for the bottom layer. As regards Cu-L edge, a slight shift in L_3 and L_2 positions occurred between top and bottom spectra (Fig. 2g), accompanied by a L_3/L_2 intensity ratio variation. Taken together, these results indicated that the bottom layer consists of Cu_2O, while the porous middle layer possesses fine structures similar to the top CuO one. Additional observations highlighted that Au NPs, mostly found in the porous copper oxide region (Fig. 3a and b), which is not on the top of the target specimen, were single-crystalline and free from any obvious clustering. As can be observed in Fig. 3c and d, their structure was consistent with that of metallic gold. EDXS chemical maps (Fig. 3e–j) demonstrated that, whereas Au NPs were dispersed within copper oxide, titanium dioxide was concentrated in relatively small regions, forming strip-shaped domains in close vicinity to Au nanoparticles (Fig. 3i and j; see also Fig. S7†). In agreement with XRD outcomes, carbon nitride turned out to be amorphous in the target specimens (see Fig. S8†).

As a matter of fact, the open morphology of the underlying copper foam substrate, along with the peculiar features of Cu_xO (consisting of a 3D array of nanowires protruding from the foam meshes) resulted in a very porous Cu_xO 3D scaffold, promoting a very close contact between the single material constituents.[30] In this regard, Au and TiO_2 in-depth dispersion was further enhanced by the inherent infiltration power of the sputtering technique,[48,49] that also triggers the diffusion of sputtered species into the innermost Cu/Cu_xO regions thanks to the continuous plasma bombardment of the growing material.[50] The synergistic concurrence of these effects, along with the (relatively) small gold and titanium dioxide amounts, resulted in the dispersion of such species in sub-surface regions that cannot be sampled by XPS, and require in fact alternative analytical techniques, as TEM, with local-probing capability on a nanometer-size scale.

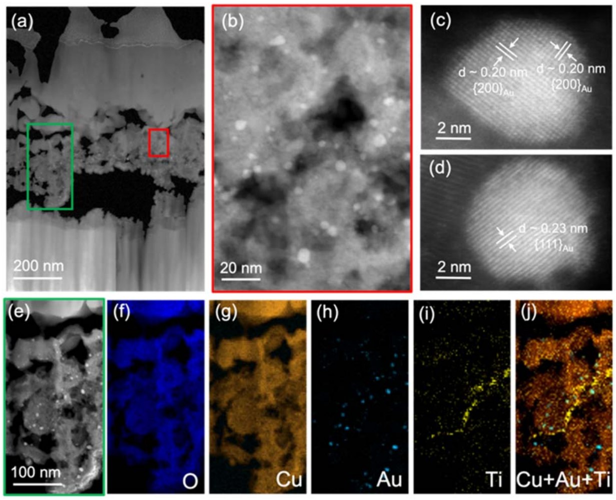

Fig. 3 (a) Overview cross-sectional STEM-ADF image for Cu_xO–gCN–TiO_2–Au. (b) STEM-ADF micrograph of the area marked by the red window in (a). Au nanoparticles (dimensions = 2÷10 nm) show a higher contrast than Cu_xO and a high image intensity, due to the relatively large atomic number of gold. (c and d) Atomic resolution STEM-ADF images of Au NPs, with indexing of gold lattice fringes and pertaining interplanar distances. The lattice fringes below the Au nanoparticle in (d) are likely coming from TiO_2. (e) STEM-ADF image of the area marked by the green box in (a), and corresponding STEM-EDXS elemental maps of O (f), Cu (g), Au (h), Ti (i), as well as the superimposed map of copper, gold, and titanium (j).

The above discussed intimate contact between the system constituents is a key issue enabling to benefit from their synergistic interplay, as showed by functional HER tests (see Fig. 4, S9, and S10†). In fact, a photocurrent density enhancement took place upon Cu_xO functionalization with gCN, TiO_2, and Au [Fig. 4a and b; see also applied bias photon-to-current efficiency (ABPE) curves in Fig. 4c] yielding, for Cu_xO–gCN–TiO_2–Au, a remarkable value of ≈ -5.7 mA cm^{-2} at 0.0 V *vs.* RHE. Such a very attractive result can be attributed to the successful formation of a high density of heterojunctions, providing various concurrent advantages: (i) a protective action towards Cu_2O, suppressing its dismutation to Cu and CuO under illumination;[2,13,19,51] (ii) an improved separation of photogenerated charge carriers, resulting in a confinement of holes in Cu_2O VB and a transfer of electrons into the CBs of the other photoelectrocatalyst constituents up to the interface with the electrolyte.[12,17,22,52,53] As a consequence, attractive performances could be achieved. In fact, the HER photocurrent onset occurred at higher potentials with respect to bare Cu_xO as soon as the junction with gCN was formed (0.32 V), and underwent further improvements after the introduction of titanium dioxide (0.34 V) and gold (0.36 V; Fig. 4d). In particular, the most active photoelectrocatalyst turned out to be Cu_xO–gCN–TiO_2–Au, for which the band structure arrangement yielded the best electron–hole separation. The resulting energy level alignment (Fig. 4e) match well with the positions of flat band potentials obtained by Mott–Schottky plots (Fig. S11†). Upon irradiation, the system components undergoing excitation are Cu_2O, CuO, and gCN, whereas Au NPs work as electron sinks with improvement of the electrical contact. The introduction of titanium dioxide, which is not excited by the adopted light source (see also Fig. S1†), exerted a protective action against photocorrosion, and enabled an improvement of photogenerated electron–hole separation, facilitating charge injection into the electrolyte.

The positive activity improvement observed upon going from Cu_xO to Cu_xO–gCN–TiO_2–Au was also confirmed by Tafel slopes (yielding, for the best performing Cu_xO–gCN–TiO_2–Au specimen, a value of ≈ -160 mV dec^{-1}; see Fig. S12†). Interestingly, the presently reported HER performances compare very favourably with those of numerous homologous electrocatalysts previously reported in the literature up to date (see Tables S1 and S2†). These characteristics, related to the unique material

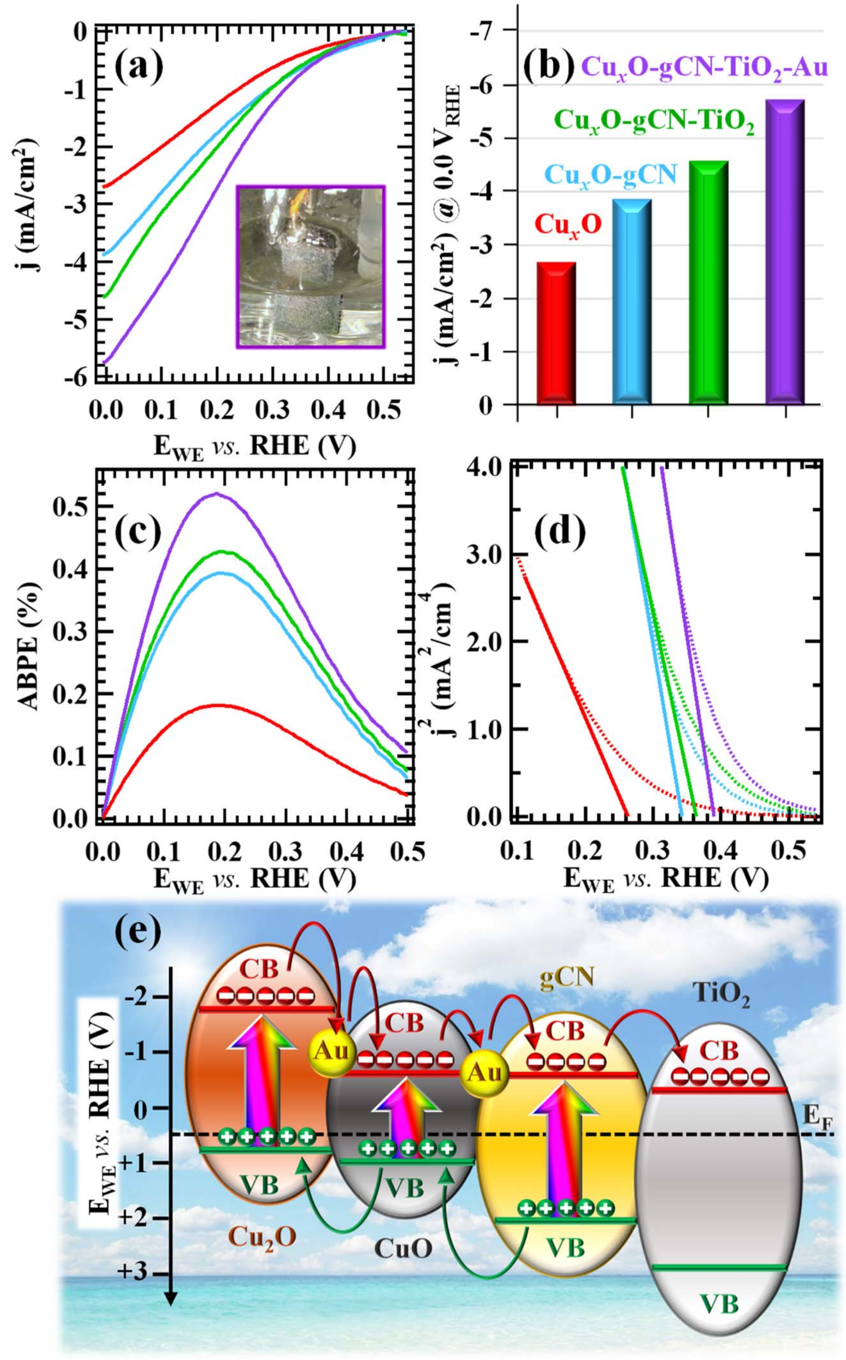

Fig. 4 Electrochemical characterization of the target photocathodes. (a) Linear-sweep voltammetry (LSV) plots of photocurrent *vs.* applied potential. Inset: Image of Cu_xO–gCN–TiO_2–Au during the LSV up to 0.0 V *vs.* RHE, evidencing the formation of H_2 bubbles. (b) Bar diagram reporting photocurrent densities at 0.0 V. (c) ABPE (%) curves. (d) Square photocurrent density (j^2) *vs.* bias curves, for Fermi level (E_F) extrapolation through the intercept with the potential axis.[47] (e) Schematic representation of the band structure arrangement for Cu_xO–gCN–TiO_2–Au. CB and VB indicate conduction and valence band edges, respectively.

morphological and compositional features (see above and ESI†), were accompanied by a very good operational stability (see Fig. S13 and S14†). This conclusion was also corroborated by post-*operando* XPS analyses, allowing to exclude the occurrence of major compositional changes upon repeated photoelectrochemical testing. In fact, neither the main photoelectron peaks (Fig. S15†; compare with Fig. 2a–d and S6†), nor quantitative analyses results (Fig. S16†) exhibited significant differences with respect to the original situation, suggesting that, differently from previously reported results,[12] no appreciable CuO conversion into Cu_2O and metallic Cu took place over time. In accordance with these outcomes, FE-SEM measurements (Fig. S17†; compare with Fig. S2c†) revealed that the system morphology did not appreciably change after functional tests, enabling thus to rule out significant degradation phenomena under operation. In perspective, this behaviour paves the way to further implementations for possible real-world end-uses, as also indicated by a preliminary proof-of-concept test aimed at bias-free photoactivated H_2 production for Cu_xO–gCN–TiO_2–Au, the best performing specimen in HER experiments. As can be observed in Fig. S18a,† after an initial induction period of ≈ 2 h, H_2 yield underwent a net increase and subsequently remained almost constant for irradiation times >20 h (mean value ≈ 1.8 mmol h^{-1} m^{-2}). This result ruled out the existence of photocorrosion processes, and highlighted an appreciable material service life. The latter feature, of notable importance for eventual practical applications,[32,54] was further confirmed by the linear trend of Fig. S18b.† The favorable activity in comparison with homologous photocatalysts, and even of Pt-containing ones (see the ESI, Pages S25–S26†), and the absence of platinum in the present supported nanosystems, that contain a minimal amount of active material,[32] render the target catalysts interesting platforms for future technological developments.

4 Conclusions

In conclusion, this work has reported on a modular and scalable route for the preparation of green Cu_xO–gCN–TiO_2–Au ($x = 1,2$) nanoarchitectures on Cu foam substrates. In particular, after the initial anodization of metallic copper foams and the liquid-phase introduction of graphitic carbon nitride, the system functionalization with titanium dioxide and gold has been accomplished by means of RF-sputtering. A careful selection of the adopted operational conditions yielded high area, multicomponent electrocatalysts, benefitting from the intimate contact of the single constituents. The synergistic chemical and electronic interplay between the latter enabled to obtain a remarkable HER activity in terms of photocurrent densities and Tafel slopes, accompanied by a very good stability. The insights provided by the present study could act as a pointer to master tailored nanoheterostructures for energy-related applications, with particular regard to the engineering of high performance photocathodes for large-scale production of green hydrogen *via* solar-activated water electrolysis. Based on the present results, optimization of material performances and detailed studies on bias-free photocatalytic hydrogen evolution from aqueous media will also be performed, in order to attain a detailed insight into the interplay between material composition and the resulting photoactivity for practical end-uses.

Author contributions

Mattia Benedet: data curation, visualization, and writing – original draft; Gian Andrea Rizzi: formal analysis, investigation and validation; Alberto Gasparotto: data analysis and validation; Lunjie Zeng: data curation and visualization; Gioele Pagot: formal analysis and investigation; Eva Olsson: funding acquisition, and writing – review & editing; Vito Di Noto: formal analysis, and writing – review & editing; Chiara Maccato: conceptualization, validation, supervision, funding acquisition, and writing – review & editing; Davide Barreca: supervision, funding acquisition, and writing.

Conflicts of interest

There are no conflicts to declare.

Acknowledgements

The present work was financially supported by Progetti di Ricerca@CNR – avviso 2020 – ASSIST, Padova University (P-DiSC#04BIRD2020-UNIPD EUREKA, P-DiSC#02BIRD2023-UNIPD RIGENERA, DOR 2021–2023), INSTM Consortium (INSTM21PDGASPAROTTO-NANOMAT, INSTM21PDBARMAC-ATENA), Supersonic Cluster beam synthesis of Innovative TRansition metal Oxides PHotoelectrodes for HYdrogen production (SCI-TROPHY) PRIN 2022 2022474YE8, CUP J53D23007340008, and the European Union's Horizon 2020 Research and Innovation Program under grant agreement no. 823717 – ESTEEM3. The authors are also very grateful to Dr G. Azzolin for valuable technical support.

References

1 S. M. Hosseini H, R. Siavash Moakhar, F. Soleimani, S. K. Sadrnezhaad, S. Masudy-Panah, R. Katal, A. Seza, N. Ghane and S. Ramakrishna, *Appl. Surf. Sci.*, 2020, **530**, 147271.

2 T. Baran, A. Visibile, M. Busch, X. He, S. Wojtyla, S. Rondinini, A. Minguzzi and A. Vertova, *Molecules*, 2021, **26**, 7271.

3 M. A. Alcudia-Ramos, M. O. Fuentez-Torres, F. Ortiz-Chi, C. G. Espinosa-González, N. Hernández-Como, D. S. García-Zaleta, M. K. Kesarla, J. G. Torres-Torres, V. Collins-Martínez and S. Godavarthi, *Ceram. Int.*, 2020, **46**, 38–45.

4 L. He, J. Liu, Y. Liu, B. Cui, B. Hu, M. Wang, K. Tian, Y. Song, S. Wu, Z. Zhang, Z. Peng and M. Du, *Appl. Catal., B*, 2019, **248**, 366–379.

5 A. M. Paul, A. Sajeev, R. Nivetha, K. Gothandapani, P. Bhardwaj, G. Karunanidhi, V. Raghavan, G. Jacob, R. Sellapan, S. K. Jeong and A. N. Grace, *Diamond Relat. Mater.*, 2020, **107**, 107899.

6 C. Lu, J. Wang, S. Czioska, H. Dong and Z. Chen, *J. Phys. Chem. C*, 2017, **121**, 25875–25881.

7 P. Karthik, T. R. Naveen Kumar and B. Neppolian, *Int. J. Hydrogen Energy*, 2020, **45**, 7541–7551.

8 L. Dai, F. Sun, P. Fu and H. Li, *RSC Adv.*, 2022, **12**, 13381–13392.

9 P. Babu, S. R. Dash and K. Parida, *J. Alloys Compd.*, 2022, **909**, 164754.

10 H. Bae, V. Burungale, W. Na, H. Rho, S. H. Kang, S.-W. Ryu and J.-S. Ha, *RSC Adv.*, 2021, **11**, 16083–16089.

11 V. Ragupathi, M. A. Raja, P. Panigrahi and N. Ganapathi Subramaniam, *Optik*, 2020, **208**, 164569.

12 R. Siavash Moakhar, S. M. Hosseini-Hosseinabad, S. Masudy-Panah, A. Seza, M. Jalali, H. Fallah-Arani,

F. Dabir, S. Gholipour, Y. Abdi, M. Bagheri-Hariri, N. Riahi-Noori, Y.-F. Lim, A. Hagfeldt and M. Saliba, *Adv. Mater.*, 2021, **33**, 2007285.

13 Y. Yang, D. Xu, Q. Wu and P. Diao, *Sci. Rep.*, 2016, **6**, 35158.

14 Z. Zhang and P. Wang, *J. Mater. Chem.*, 2012, **22**, 2456–2464.

15 R. A. Rather, S. Singh and B. Pal, *Appl. Catal., B*, 2017, **213**, 9–17.

16 X. Ma, J. Zhang, B. Wang, Q. Li and S. Chu, *Appl. Surf. Sci.*, 2018, **427**, 907–916.

17 Y. Wang, S. Cao, Y. Huan, T. Nie, Z. Ji, Z. Bai, X. Cheng, J. Xi and X. Yan, *Appl. Surf. Sci.*, 2020, **526**, 146700.

18 B. Chen, J. Yu, R. Wang, X. Zhang, B. He, J. Jin, H. Wang and Y. Gong, *Sci. China Mater.*, 2022, **65**, 139–146.

19 S. Wojtyła and T. Baran, *Nano Sel.*, 2021, **2**, 389–397.

20 A. Paracchino, V. Laporte, K. Sivula, M. Grätzel and E. Thimsen, *Nat. Mater.*, 2011, **10**, 456–461.

21 W. Srevarit, S. Moonmangmee, P. Phapugrangkul, S. Kuboon, A. Klamchuen, N. Saito and C. Ponchio, *J. Alloys Compd.*, 2021, **859**, 157818.

22 J. Li, X. Jin, R. Li, Y. Zhao, X. Wang, X. Liu and H. Jiao, *Appl. Catal., B*, 2019, **240**, 1–8.

23 S. Masudy-Panah, R. Siavash Moakhar, C. S. Chua, A. Kushwaha and G. K. Dalapati, *ACS Appl. Mater. Interfaces*, 2017, **9**, 27596–27606.

24 M. Benedet, A. Gallo, C. Maccato, G. A. Rizzi, D. Barreca, O. I. Lebedev, E. Modin, R. McGlynn, D. Mariotti and A. Gasparotto, *ACS Appl. Mater. Interfaces*, 2023, **15**, 47368–47380.

25 Y. Zou, J.-W. Shi, D. Ma, Z. Fan, C. Niu and L. Wang, *ChemCatChem*, 2017, **9**, 3752–3761.

26 S. Samanta, S. Martha and K. Parida, *ChemCatChem*, 2014, **6**, 1453–1462.

27 S. A. Ladva, W. Travis, R. Quesada-Cabrera, M. Rosillo-Lopez, A. Afandi, Y. Li, R. B. Jackman, J. C. Bear, I. P. Parkin, C. Blackman, C. G. Salzmann and R. G. Palgrave, *Nanoscale*, 2017, **9**, 16586–16590.

28 Y. Fang, W. Huang, S. Yang, X. Zhou, C. Ge, Q. Gao, Y. Fang and S. Zhang, *Int. J. Hydrogen Energy*, 2020, **45**, 17378–17387.

29 P. P. Singh and V. Srivastava, *RSC Adv.*, 2022, **12**, 18245–18265.

30 L. Bigiani, T. Andreu, C. Maccato, E. Fois, A. Gasparotto, C. Sada, G. Tabacchi, D. Krishnan, J. Verbeeck, J. R. Morante and D. Barreca, *J. Mater. Chem. A*, 2020, **8**, 16902–16907.

31 M. Li, Z. Wang, Q. Zhang, C. Qin, A. Inoue and W. Guo, *Appl. Surf. Sci.*, 2020, **506**, 144819.

32 D. Barreca, G. Carraro, A. Gasparotto, C. Maccato, M. E. A. Warwick, E. Toniato, V. Gombac, C. Sada, S. Turner, G. Van Tendeloo and P. Fornasiero, *Adv. Mater. Interfaces*, 2016, **3**, 1600348.

33 Z. Wang, Y. Zhang, H. Xiong, C. Qin, W. Zhao and X. Liu, *Sci. Rep.*, 2018, **8**, 6530.

34 D. Briggs and M. P. Seah, *Practical Surface Analysis: Auger and X-Ray Photoelectron Spectroscopy*, New York, NY, Wiley, 2nd edn, 1990.

35 O. Baranov, M. Košiček, G. Filipič and U. Cvelbar, *Appl. Surf. Sci.*, 2021, **566**, 150619.

36 O. Baranov, K. Bazaka, T. Belmonte, C. Riccardi, H. E. Roman, M. Mohandas, S. Xu, U. Cvelbar and I. Levchenko, *Nanoscale Horiz.*, 2023, **8**, 568–602.

37 X. Shu, H. Zheng, G. Xu, J. Zhao, L. Cui, J. Cui, Y. Qin, Y. Wang, Y. Zhang and Y. Wu, *Appl. Surf. Sci.*, 2017, **412**, 505–516.

38 Y. Qu, P. Zhang, J. Liu, L. Zhao, X. Song and L. Gao, *Mater. Chem. Phys.*, 2019, **226**, 88–94.

39 Y. Wang, T. Jiang, D. Meng, H. Jin and M. Yu, *Appl. Surf. Sci.*, 2015, **349**, 636–643.

40 L. Armelao, D. Barreca, M. Bertapelle, G. Bottaro, C. Sada and E. Tondello, *Thin Solid Films*, 2003, **442**, 48–52.

41 D. Barreca, A. Gasparotto and E. Tondello, *Surf. Sci. Spectra*, 2009, **14**, 41–51.

42 D. Barreca, A. Gasparotto, C. Maccato, E. Tondello, O. I. Lebedev and G. Van Tendeloo, *Cryst. Growth Des.*, 2009, **9**, 2470–2480.

43 J. F. Moulder, W. F. Stickle, P. E. Sobol and K. D. Bomben, *Handbook of X-Ray Photoelectron Spectroscopy*, Perkin Elmer Corporation, Eden Prairie, MN, USA, 1992.

44 L. Laffont, M. Y. Wu, F. Chevallier, P. Poizot, M. Morcrette and J. M. Tarascon, *Micron*, 2006, **37**, 459–464.

45 X. Xie, X. Fan, X. Huang, T. Wang and J. He, *RSC Adv.*, 2016, **6**, 9916–9922.

46 R. F. Egerton, *Electron Energy-Loss Spectroscopy in the Electron Microscope*, New York, NY, Springer, 3rd edn, 2011.

47 J. C. Alexander, *Surface Modifications and Growth of Titanium Dioxide for Photo-Electrochemical Water Splitting*, Springer Theses, 2016.

48 M. Benedet, G. A. Rizzi, A. Gasparotto, O. I. Lebedev, L. Girardi, C. Maccato and D. Barreca, *Chem. Eng. J.*, 2022, **448**, 137645.

49 M. Benedet, G. A. Rizzi, A. Gasparotto, N. Gauquelin, A. Orekhov, J. Verbeeck, C. Maccato and D. Barreca, *Appl. Surf. Sci.*, 2023, **618**, 156652.

50 A. Gasparotto, D. Barreca, D. Bekermann, A. Devi, R. A. Fischer, C. Maccato and E. Tondello, *J. Nanosci. Nanotechnol.*, 2011, **11**, 8206–8213.

51 T. Xie, T. Zheng, R. Wang, Y. Bu and J.-P. Ao, *Green Energy Environ.*, 2018, **3**, 239–246.

52 W. Niu, T. Moehl, W. Cui, R. Wick-Joliat, L. Zhu and S. D. Tilley, *Adv. Energy Mater.*, 2018, **8**, 1702323.

53 M. A. Lumley, A. Radmilovic, Y. J. Jang, A. E. Lindberg and K.-S. Choi, *J. Am. Chem. Soc.*, 2019, **141**, 18358–18369.

54 D. Barreca, G. Carraro, V. Gombac, A. Gasparotto, C. Maccato, P. Fornasiero and E. Tondello, *Adv. Funct. Mater.*, 2011, **21**, 2611–2623.